Regulation of actomyosin contraction as a driving force of invasive lobular breast cancer

Schipper, K.

Truncated ASPP2 drives initiation and progression of invasive lobular carcinoma via distinct mechanisms

4

Koen Schipper[1], Anne Paulien Drenth[1], Eline van der Burg[1], Samuel P. Cornelissen[1], Sjoerd Klarenbeek[2], Micha Nethe[1,3*], Jos Jonkers[1*]

1 Division of Molecular Pathology, Oncode Institute, The Netherlands Cancer Institute, Amsterdam, The Netherlands

2 Experimental Animal Pathology, The Netherlands Cancer Institute, Amsterdam, the Netherlands.

3 Present address: Department of Hematopoiesis, Sanquin Research and Landsteiner Laboratory, Academic Medical Center, Amsterdam, The Netherlands

Published in Cancer Research, 1 April 2020
Volume 80, Issue 7, pages 1486-1497

Abstract

Invasive lobular carcinoma (ILC) accounts for 8-14% of all breast cancer cases. The main hallmark of ILCs is the functional loss of the cell-cell adhesion protein E-cadherin. Nonetheless, loss of E-cadherin alone does not predispose mice to mammary tumor development indicating that additional perturbations are required for ILC formation. Previously, we identified an N-terminal truncation variant of ASPP2 (t-ASPP2) as a driver of ILC in mice with mammary-specific loss of E-cadherin. Here we showed that expression of t-ASPP2 induced actomyosin relaxation, enabling adhesion and survival of E-cadherin-deficient murine mammary epithelial cells on stiff matrices like fibrillar collagen. The induction of actomyosin relaxation by t-ASPP2 was dependent on its interaction with protein phosphatase 1 (PP1) but not on t-ASPP2-induced YAP activation. Truncated ASPP2 collaborated with both E-cadherin loss and PI3K pathway activation via PTEN loss in ILC development. t-ASPP2-induced actomyosin relaxation was required for ILC initiation but not progression. Conversely, YAP activation induced by t-ASPP2 contributed to tumor growth and progression while being dispensable for tumor initiation. Together these findings highlight two distinct mechanisms through which t-ASPP2 promotes ILC initiation and progression.

Introduction

Breast cancer is the most frequent cancer type in women worldwide. Invasive lobular carcinoma (ILC) is the second most common breast cancer subtype, accounting for 8-14% of all breast cancer cases[1–3]. ILCs typically display a discohesive morphology caused by functional loss of the intercellular adhesion protein E-cadherin (encoded by *CDH1*)[4]. Loss of E-cadherin in mammary epithelium drives cell extrusion of luminal epithelial cells into the surrounding mammary stroma and underlies the strong infiltrative nature of ILC[5]. The highly infiltrative nature of ILCs typically complicates early detection and surgical removal[6]. Loss of E-cadherin is typically achieved by inactivating mutations, loss of heterozygosity (LOH) or functional loss of members of the E-cadherin–catenin complex[4,7–9]. Although loss of E-cadherin is the most common alteration in ILCs, loss of E-cadherin by itself is insufficient to drive tumorigenesis in mice[10–13].

To identify driver mutations that cooperate with E-cadherin loss in ILC

formation, we have previously performed a transposon-based insertional mutagenesis screen in mice with mammary-specific inactivation of E-cadherin[14]. We identified *Mypt1/2* (also known as *Ppp1r12a/b*), *Aspp2* (also known as *Trp53bp2*) and *Myh9* as novel drivers of ILC. Intriguingly, transposon insertions in these genes were mutually exclusive indicating a shared underlying mechanism. MYPT1/2 and ASPP2 are binding partners of protein phosphatase 1 (PP1) that regulate the specificity of PP1. While MYPT1 and MYPT 2 are primarily known to regulate myosin light chain (MLC) activity, ASPP2 has been shown to regulate the activity of the transcription factors YAP and TAZ. In addition to PP1 binding[15–17], ASPP2 has several other binding partners including p53, BCL2 and RelA/p65[18]. MYH9 is the heavy chain of the non-muscle myosin IIa complex, which is responsible for actomyosin contraction[19]. MYH9 has previously been identified as a tumor suppressor, but there are conflicting findings regarding the mechanism through which MYH9 loss results in tumor formation[14,20,21]. Transposon insertions in *Mypt1/2* and *Aspp2* resulted in the expression of C- and N-terminally truncated proteins, respectively, while heterozygous insertions in *Myh9* caused reduced expression of MYH9[14]. The MYPT1 and ASPP2 truncation variants both retain their PP1 binding motif indicating that this interaction might be important for their ability to induce ILC. In addition, both MYPT1 and ASPP2 truncation variants lack negative regulatory domains indicating that these truncations are dominant-active variants[5,22,23]. We found that expression of truncated MYPT1 and inhibition of MYH9 induces ILC formation by reducing actomyosin contractility in E-cadherin-deficient murine mammary epithelial cells (MMECs)[5]. Reduction of actomyosin contraction enables E-cadherin-deficient MMECs to adhere and grow on stiff matrixes like fibrillar collagen[5]. Fibrillar collagen is an extracellular matrix component highly abundant in ILC[24]. While it is well known that MYPT1/2 and MYH9 play important roles in actomyosin contractility, ASPP2 has not been implicated in the regulation of this pathway[19]. ASPP2 was originally discovered as a protein that can bind and facilitate p53-mediated apoptosis[25–27]. However, the functions of ASPP2 are not limited to p53 regulation. Since its discovery, ASPP2 has been shown to play important roles in diverse cellular processes ranging from chromosome segregation to cell polarity[16,17,28–30]. Overall, it remains unclear by which mechanism truncated ASPP2 drives ILC development. In this study we therefore investigated how the previously identified truncation variant of ASPP2 drives ILC formation, how tumors induced by truncated ASPP2 progress, and if truncated ASPP2 cooperates with other drivers in ILC development.

Materials and Methods

Generation of mice

The generation of *WapCre;Cdh1$^{F/F}$, WapCre;Cdh1$^{F/F}$;Col1a1$^{invCAG\text{-}Ppp1r12a\text{-}ex1\text{-}9\text{-}IRES\text{-}Luc/+}$* (WE$^{F/F}$;t-MYPT1) ,*WapCre;Cdh1$^{F/F}$;Col1a1$^{invCAG\text{-}Trp53bp2\text{-}ex13\text{-}18\text{-}IRES\text{-}Luc/+}$* (WE$^{F/F}$;t-ASPP2) and *WapCre;Cdh1$^{F/F}$;Pten$^{F/F}$* (WE$^{F/F}$;PTEN$^{F/F}$) mice were previously described[11,13,14]. *WapCre;Cdh1$^{F/F}$;Pten$^{F/F}$;Col1a1$^{invCAG\text{-}Ppp1r12a\text{-}ex1\text{-}9\text{-}IRES\text{-}Luc/+}$* (WE$^{F/F}$;PTEN$^{F/F}$;t-MYPT1) and *WapCre;Cdh1$^{F/F}$;Pten$^{F/F}$;Col1a1$^{invCAG\text{-}Trp53bp2\text{-}ex13\text{-}18\text{-}IRES\text{-}Luc/+}$* (WE$^{F/F}$;PTEN$^{F/F}$;t-ASPP2) mice were generated by crossing WE$^{F/F}$;t-MYPT1 and WE$^{F/F}$;t-ASPP2 mice with WE$^{F/F}$;PTEN$^{F/F}$ mice. Mice were palpated weekly for the development of mammary tumors after weaning. For these experiments, no statistical tests were performed to determine the sample size with the exception of the experiment described in Fig 3A, for which the average mammary tumor free (MTS) survival and standard deviation observed in Fig 2B were used to determine the sample size required to determine a minimum change in average MTS of 20%. Investigators were not blinded to the genetic background of animals. Multiplex genotyping of animals was performed using the Qiaxcel (Qiagen) with the primers found in Supplementary Table 1. All animal experiments were approved by the Animal Ethics Committee of the Netherlands Cancer Institute and performed in accordance with institutional, national and European guidelines for Animal Care and Use.

GSK-269962 intervention study

Female WE$^{F/F}$ mice were treated with Vehicle (6% Hydroxypropyl-β-Cyclodextrin, pH 4.0 (Sigma) and 5% DMSO in demineralized water) or GSK-269962 (2 or 6 mg/kg (Medkoo)) daily by oral gavage starting at 5 weeks of age. The treatment group for each mouse was randomly assigned. The volume administered was 10 µL/g bodyweight of the mouse. The mice were weighed daily and palpated once a week to monitor mammary tumor formation. For a subset of mice, the treatment had to be temporarily suspended due to unexpected weight loss (Supplementary Table 2). Twenty weeks after the start of the experiment the mice were sacrificed and tumor burden was quantified by dividing the tumor surface area by the total mammary gland surface area.

In vivo bioluminescence imaging

In vivo bioluminescence imaging was performed as previously described[31]. The animals were imaged from the age of 4 weeks every 2 to 8 weeks depending on the age of the animal. Quantification of signal intensity was performed over the region of interest and quantified as flux (photons per second per square centimeter per steradian).

Intraductal injection of lentivirus and assessment of tumor development

Intraductal injections were performed as previously described[32,33]. Briefly, $WE^{F/F}$ mice (2-5 months of age) were anesthetized using ketamine/sedazine (100 and 10 mg/kg respectively) and hair was removed from the nipple area with a commercially available hair removal cream. Eighteen µL of high-titer lentivirus mixed with 2 µL 0.2% Evans blue dye in PBS was injected in the fourth mammary glands by using a 34G needle. Mice were handled in a biological safety cabinet under a stereoscope. Lentiviral titers ranging from 2x10^8 TU/mL to 2x10^9 TU/mL were used. Animals were sacrificed at 20 weeks post-injection. Tumor burden was quantified by dividing the tumor surface area by the total mammary gland surface area using H&E stained slides.

Lentiviral vectors and virus production

Generation of SIN.LV.SF-GFP-T2A-puro, SIN.LV.SF-T2A-puro (Empty Vector Fig. 6a) and SIN.LV.SF- tMYPT1-T2A-puro was previously described[14]. t-ASPP2 was isolated with Age1-Sal1 or BamH1-Age1 overhangs and a 5' FLAG tag from the *Trp53bp2*$^{ex13\text{-}18}$ pBABE puro vector previously described[14] using Phusion Flash High-Fidelity DNA Polymerase (Thermo scientific). The cDNA fragments were then inserted into SIN.LV.SF[34] or SIN.LV.SF-T2A-puro to generate SIN.LV.SF-t-ASPP2 and SIN.LV.SF- tASPP2-T2A-puro. T2-ASPP2 was isolated with BamH1-Age1 or BamH1-Sal1 overhangs and a 5' FLAG tag from SIN.LV.SF tASPP2 using Phusion Flash High-Fidelity DNA Polymerase. The cDNA fragments were then inserted into SIN.LV.SF or SIN.LV.SF-T2A-puro to generate SIN.LV.SF t2-ASPP2 and SIN.LV.SF-t2-ASPP2-T2A-puro. SIN.LV.SF-t-$ASPP2^{\Delta YAP}$-T2A-puro and SIN.LV.SF-t-$ASPP2^{\Delta PP1}$-T2A-puro were generated by site directed mutagenesis using the QuikChange Lightning site directed mutagenesis kit (Agilent). All primers are listed in Supplementary Table 1. Every vector was validated by Sanger sequencing. Concentrated lentiviral stocks were produced by transient co-transfection of four plasmids in 293T cells as previously described[33]. Viral titers were

determined using the qPCR lentivirus titration kit from Abm (LV900).

Cell culture

The generation WE$^{F/F}$;mTmG primary mouse mammary epithelial cell (MMEC) clones was described previously[5]. WE$^{F/F}$;mTmG MMECs were cultured in Dulbecco's modified Eagle's medium (DMEM)-F12 (10565–018; Gibco) supplemented with 10% FBS, 1% penicillin-streptomycin, 5 ng/mL epidermal growth factor (EGF) (Sigma), 5ng/ml insulin (all from Life Technologies) and 5 ng/ml cholera toxin (Gentaur). Y-27632 (10 μM, Abmole, M1817) was added to the cell culture medium when indicated. All MMEC lines were regularly tested for mycoplasma contamination.

Colony formation assays

WE$^{F/F}$;mTmG MMECs were plated at a density of 5000 cells per well in 6-well plates in the presence or absence of the ROCK inhibitor Y-27632 (10 μM). Seven days after plating the cells were fixated using 4% formaldehyde for 15 minutes and stained with 0.5% crystal violet dissolved in 25% methanol for at least 30 minutes at room temperature. The plates were then washed three times with demineralized water to remove any unbound dye and dried at room temperature in the dark. The crystal violet stainings were imaged using the Gel count (Oxford Optronix) and analysed using its respective software. Quantification was performed by dissolving the crystal violet in 10% acetic acid in demineralized water and measuring the absorbance at 560 nm. The absorbance was normalized to the indicated control samples.

Immunofluorescence

Formalin-fixed and paraffin-embedded sections were processed as previously described[11] and incubated overnight at 4°C with primary antibodies against Cytokeratin 8 (1:200, DSHB Troma-1), E-cadherin (1:200, E-bioscience #610181) or Ki67 (1:100, Cell Signalling # 9129). Secondary antibodies anti-Mouse-AlexaFluor 647 (1:1000, Invitrogen #A28181), anti-Rabbit-AlexaFluor 488 (1:1000, Invitrogen #A27034), anti-Rat-AlexaFluor 568 (1:1000, Invitrogen #A11077), were incubated overnight at 4°C. Sections were subsequently stained with Hoechst (1:1000, Thermo Scientific #62249) for 5 min and mounted using Vectashield (Vector Laboratories H-1000). Cultured MMECs were fixed with 4% paraformaldehyde (PFA) and stained with a primary antibody against: pMLC (1:100, Cell Signaling #3675)

overnight at 4 degrees. The cells were then stained with the secondary antibody anti-Rabbit-Alexa Fluor 568 (1:1000, Invitrogen #A11011), Alexa Fluor™ 647 Phalloidin (Thermo Fisher, A22287) and if indicated Hoechst (1:1000. Thermos Fischer, 62249), for 1 hour at room temperature. All images were acquired using a Leica TCS SP5 Confocal and analyzed using LAS AF Version 2.6.3 software. For the merged images the pMLC signal was depicted in green and the phalloidin signal was depicted in Red. pMLC stainings were quantified using ImageJ and normalized to the GFP surface area.

Western blot analysis

Western blot experiments were conducted as described previously[14]. The following primary antibodies were used to determine protein expression by Western blot: FLAG (1:5000, Sigma F7425), YAP (1:1000, Cell Signaling, #4912), phospho YAP (Ser127) (1:1000, Cell Signaling, #4911), and β-actin (1:20000, Sigma, #A5441).The following secondary antibodies were used: Anti-Rabbit HRP (1:2000, DAKO, P0260), Anti-Mouse HRP (1:2000, DAKO, P0448) and Anti-mouse IRDye 680nm (1:5000, Li-COR 926-32222).

Histopathology

Mouse tissues were formalin-fixed in 10% neutral buffered formalin for 48 hours, embedded in paraffin, sectioned and stained with hematoxylin and eosin (H&E). Immunohistochemistry (IHC) was performed as previously described[31]. All slides were digitally processed using the Aperio ScanScope (Aperio, Vista, CA, USA) and captured using ImageScope software version 12.0.0 (Aperio). The histopathological classification of tumors shown in supplementary figure 2 was performed based on the criteria described in Supplementary table 3.

Statistical analyses

Graphpad Prism v7.03 was used to generate all graphs and perform the statistical analyses. All graph data is represented as mean and standard deviations. Survival probabilities were estimated using the Kaplan–Meier method and compared using the Mantel–Cox test. All other *p*-values were calculated using an unpaired two tailed t-test. *P* values < 0.05 were considered significant.

Results

t-ASPP2 induces actomyosin relaxation enabling adhesion and survival of E-cadherin-deficient MMECs

We have previously shown that E-cadherin-deficient MMECs derived from *Wcre;Cdh1$^{F/F}$;mTmG* mice are able to adhere and survive on stiff matrixes such as collagen or uncoated plastic culture dishes by reducing their actomyosin contractility[5]. ROCK inhibition (Y-27632) or expression of truncated MYPT1 (t-MYPT1) partially reduced actomyosin contractility thereby allowing cell expansion of E-cadherin-deficient MMECs *in vitro*. The observed mutual exclusivity of the transposon insertions in *Aspp2, Mypt1*/2 and *Myh9* suggests that expression of truncated ASPP2 (t-ASPP2) also affects actomyosin contractility[14]. To test this hypothesis, we overexpressed t-ASPP2, t-MYPT1 or GFP (used as control) in E-cadherin-deficient MMECs (Fig. 1a and b). Colony formation assays showed that expression of t-ASPP2 or t-MYPT1 drives cell expansion of E-cadherin-deficient MMECs and obviates the need to add ROCK inhibitors to the culture medium to enable cell adhesion (Fig. 1c and d). It is well known that MYPT1 drives MLC dephosphorylation by forming a complex with PP1[35]. We previously showed that t-MYPT1 dephosphorylates MLC at Serine 19 and has a higher activity than wild type MYPT1[5]. Also t-ASPP2 is predicted to have higher activity than wild type ASPP2 because it lacks the proline-rich domain that is known to inhibit protein-protein interactions of ASPP2 by masking the C-terminal ankyrin and SH3 domains (Fig. 1a)[22]. We therefore hypothesized that t-ASPP2 may enable adhesion and survival of E-cadherin-deficient MMECs on stiff matrixes by reducing actomyosin contractility similar to t-MYPT1. To test this hypothesis, we measured MLC phosphorylation by immunofluorescence (IF) analysis of E-cadherin-deficient MMECs expressing t-ASPP2, t-MYPT1, or GFP (Fig. 1e and f). This revealed that t-ASPP2 drives MLC dephosphorylation to comparable levels as t-MYPT1 (Fig. 1e, f). Altogether, these results show that t-ASPP2 drives actomyosin relaxation, enabling adhesion and survival of E-cadherin-deficient MMECs on stiff surfaces.

t-ASPP2 drives ILC development by inducing actomyosin relaxation

To validate t-MYPT1 and t-ASPP2 as drivers of ILC, we have previously generated the *Wap–Cre*;*Cdh1$^{F/F}$*;*Col1a1$^{invCAG\text{-}Ppp1r12a\text{-}ex1\text{-}9\text{-}IRES\text{-}Luc/+}$* (hereafter

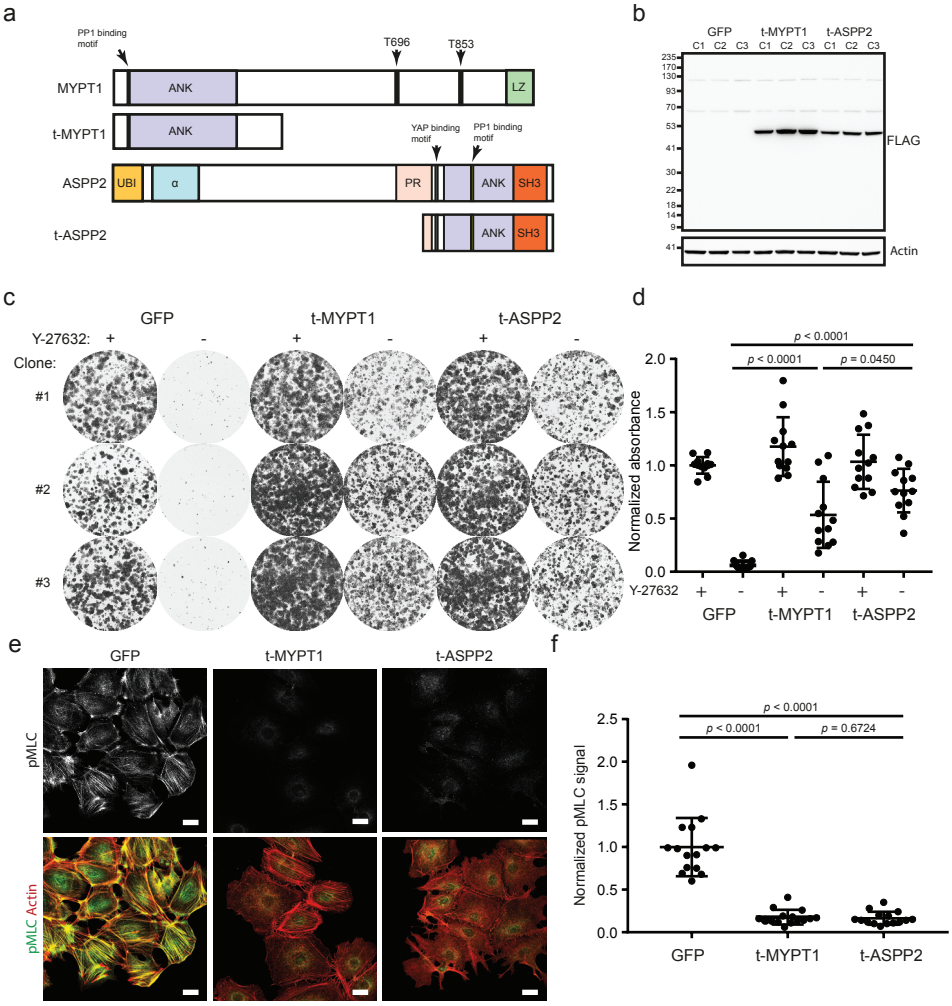

Figure 1: t-ASPP2 induces actomyosin relaxation enabling adhesion and survival of E-cadherin-deficient MMECs (**a**) Schematic overview of MYPT1 and ASPP2 truncation variants compared to WT MYPT1 and ASPP2. UBL: ubiquitin-like domain, α-helical: α-helical domain, PRO: proline-rich domain, PP1: PP1-binding domain, ANK: ankyrin repeats, SH3: Src homology 3 domain, LZ: leucine zipper. (**b**) Western blot analysis of WE$^{F/F}$;*mTmG* MMECs transduced with t-MYPT1 and t-ASPP2 or GFP stained for FLAG. (**c**, **d**) Representative images (**c**) and quantification (**d**) of clonogenic assays with WE$^{F/F}$;*mTmG* MMECs transduced with MYPT1$^{1\text{-}413}$, ASPP2$^{766\text{-}1134}$ or GFP 7 days after seeding the cells in the presence or absence of 10 μM Y-27632. (**e**, **f**) IF staining (**e**) and quantification (**f**) of WE$^{F/F}$;*mTmG* MMECs transduced with t-MYPT1 and t-ASPP2 or GFP 48 hours post washout of 10 μM Y-27632 stained for phospho myosin light chain (serine 19), and actin. Scale bar is 25 μm.

referred to as WE$^{F/F}$;t-MYPT1) and *Wap–Cre*;*Cdh1*$^{F/F}$;*Col1a1*$^{invCAG\text{-}Trp53bp2\text{-}ex13\text{-}18\text{-}IRES\text{-}Luc/+}$ (hereafter referred to as WE$^{F/F}$;t-ASPP2) mouse models, which combine mammary-specific loss of E-cadherin with overexpression of

either t-MYPT1 or t-ASPP2 (Fig. 2a)[14]. Both WE$^{F/F}$;t-MYPT1 and WE$^{F/F}$;t-ASPP2 female mice showed mammary-specific bioluminescence, indicating that t-MYPT1 and t-ASPP2 are expressed (Supplementary Fig. 1a-c). To study tumor onset and progression, we set up tumor watch cohorts. In line with previous results, we observed tumor development in both WE$^{F/F}$;t-MYPT1 and WE$^{F/F}$;t-ASPP2 mice with similar median tumor-free latencies (T50) of 103 and 98 days, respectively (Fig. 2b). Compared to WE$^{F/+}$;t-MYPT1 mice, all WE$^{F/+}$;t-ASPP2 mice developed palpable tumors during their lifespan and with significant shorter T50 of 261 versus 357 days, respectively (Fig. 2c). Most mammary tumors derived from WE$^{F/F}$;t-MYPT1 and WE$^{F/F}$;t-ASPP2 mice had a classical mouse ILC morphology as reported earlier (Supplementary Fig. 2a, b)[14]. Tumors derived from WE$^{F/+}$;t-MYPT1 and WE$^{F/+}$;t-ASPP2 mice generally retained membranous E-cadherin expression, indicating that no LOH occurred in those tumors (Supplementary Fig. 2a, B). Despite the lack of LOH, the tumors derived from WE$^{F/+}$;t-MYPT1 and WE$^{F/+}$;t-ASPP2 mice were very rich in collagen similar to their E-cadherin-deficient counterparts (Supplementary Fig. 2). To provide further evidence that actomyosin relaxation caused by t-MYPT1 or t-ASPP2 collaborates with E-cadherin loss in mammary tumor development, we orally treated female WE$^{F/F}$ mice daily for 20 weeks with the ROCK inhibitor GSK-269962, which is more potent, more specific and has a better oral bioavailability than Y-27632 (Fig. 2d)[36,37]. Only mice treated with the higher dose (6 mg/kg) of GSK-269962 developed tumors that resembled tumors arising in WE$^{F/F}$;t-MYPT1 and WE$^{F/F}$;t-ASPP2 mice (Fig. 2e and f). Determination of plasma levels of GSK-269962 at the start of the experiment and 4 weeks after the start showed that there is no accumulation of GSK-269962 over time (Supplementary *Fig.* 3a, b). Additionally, oral dosing of mice with 2 mg/kg GSK-269962 resulted in rapid drug excretion within 8 hours after administration potentially explaining the lack of tumor formation in this treatment group (Supplementary Fig. 3). Overall, these data show that actomyosin relaxation induced by t-ASPP2 or ROCK inhibitors collaborates with loss of E-cadherin in ILC development.

Actomyosin relaxation cooperates with PI3 kinase pathway activation to enhance tumor initiation and growth.

In ILC, the most common somatic mutations (next to E-cadherin loss) are found in members of phosphoinositol-3 kinase (PI3K) pathway, such as PIK3CA and PTEN[9,38,39]. We and others have shown in mice that mammary-specific loss of E-cadherin in combination with loss of PTEN or expression

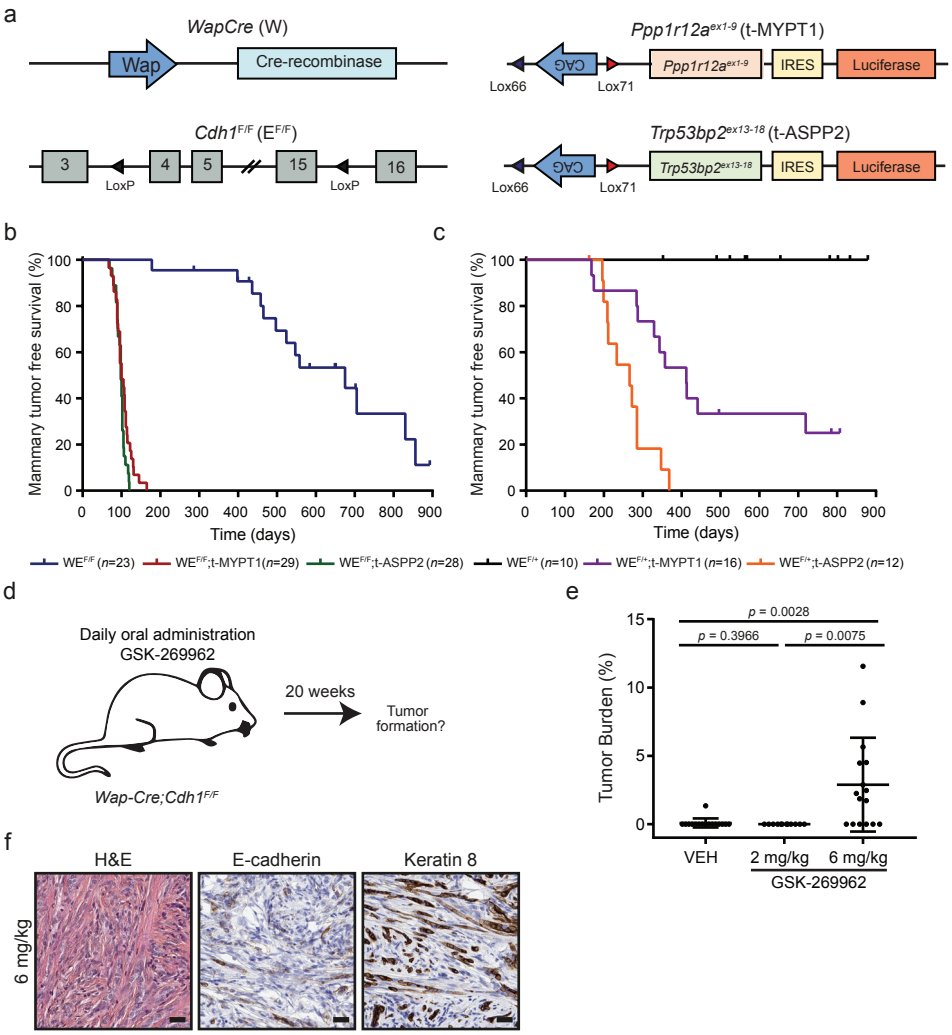

Figure 2: t-ASPP2 drives ILC development by inducing actomyosin relaxation (**a**) Overview of the engineered alleles in the *Wcre*;*Cdh1*$^{F/F}$;*Ppp1r12A*$^{ex1-9}$ (WE$^{F/F}$;t-MYPT1), and *Wcre*;*Cdh1*$^{F/F}$;*Trp53bp2*$^{Ex13-18}$ (WE$^{F/F}$;t-ASPP2) mice. (**b**, **c**) Kaplan–Meier curves showing mammary tumor-free survival for female mice with the indicated genotypes. (**d**) Study design of *in vivo* intervention study with the ROCK inhibitor GSK-269962. WE$^{F/F}$ mice were orally treated with 2 or 6 mg/kg GSK-269962 or Vehicle daily for 140 days. (**e**) Tumor burden of WE$^{F/F}$ female mice treated with Vehicle (n = 4), 2 mg/kg GSK-269962 (n = 3), 6 mg/kg GSK-269962 (n = 4). (**f**) Representative images for H&E staining (left) and for expression of E-cadherin (middle) and CK8 (right) in tumors of mice treated with 6 mg/kg GSK-269962. Scale bar is 25 µm.

of mutant PIK3CA leads to development of tumors that closely resemble classic ILC[11,33,40]. We therefore wondered if actomyosin relaxation might enhance ILC development induced by E-cadherin loss and PI3K pathway

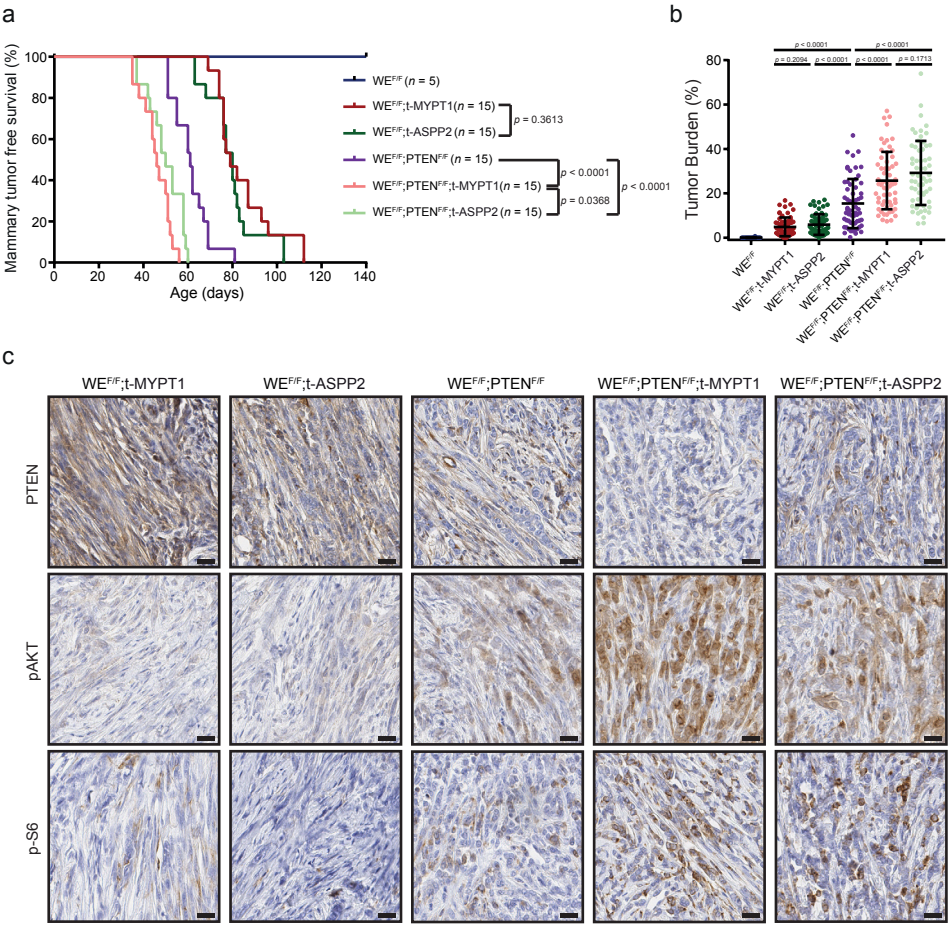

Figure 3: Actomyosin relaxation cooperates with PI3 kinase pathway activation to enhance tumor initiation and growth (**a**) Kaplan–Meier analysis showing mammary tumor-free survival for the indicated genotypes. (**b**) Tumor burden of mammary glands of female mice with the indicated genotyped at the age of 20 weeks. (**c**) Representative images for IHC stainings of mammary tumors from 20 week old female mice with the indicated genotypes stained for PTEN, phospho AKT and phospho S6. Scale bars are 20 µm.

activation. To address this question, we crossed WE$^{F/F}$;t-MYPT1 and WE$^{F/F}$;t-ASPP2 mice with *WapCre;Cdh1$^{F/F}$;Pten$^{F/F}$* (WE$^{F/F}$;PTEN$^{F/F}$) mice to generate WE$^{F/F}$;PTEN$^{F/F}$;t-MYPT1 and WE$^{F/F}$;PTEN$^{F/F}$;t-ASPP2 female mice, which were monitored for mammary tumor development (Fig. 3a). With the exception of WE$^{F/F}$ mice, all mice developed mammary tumors within 140 days. WE$^{F/F}$;PTEN$^{F/F}$ mice (T50 = 60 days) developed mammary tumors faster than WE$^{F/F}$;t-MYPT1 mice (T50 = 83 days) and WE$^{F/F}$;t-ASPP2 mice (T50 = 80 days) (Fig. 3a). Intriguingly, WE$^{F/F}$;PTEN$^{F/F}$;t-MYPT1 mice (T50 = 46 days) and WE$^{F/F}$;PTEN$^{F/F}$;t-ASPP2 mice (T50 = 50 days) developed tumors

significantly faster than $WE^{F/F}$;$PTEN^{F/F}$ mice, showing that expression of t-MYPT1 or t-ASPP2 enhances mammary tumor formation induced by loss of E-cadherin and PTEN (Fig. 3a). $WE^{F/F}$;$PTEN^{F/F}$;t-MYPT1 and $WE^{F/F}$;$PTEN^{F/F}$;t-ASPP2 mice also showed a higher tumor burden compared to $WE^{F/F}$;$PTEN^{F/F}$ mice, indicating that actomyosin relaxation collaborates with PTEN loss in mammary tumorigenesis (Fig. 3b). Tumors from $WE^{F/F}$;$PTEN^{F/F}$;t-MYPT1 and $WE^{F/F}$; $PTEN^{F/F}$;t-ASPP2 mice were similar to tumors from $WE^{F/F}$;$PTEN^{F/F}$ mice, showing ILC morphologies, expression of keratin 8, lack of E-cadherin and PTEN expression, and high abundance of fibrillar collagen (Supplementary Fig. 4). Increased phosphorylation of AKT (Serine 437) and S6 ribosomal protein (Serine 435 and 436) in the tumors harboring loss of PTEN indicates that these tumors have increased canonical PI3K signaling (Fig. 3c). Altogether, these data show that actomyosin relaxation cooperates with E-cadherin loss and PI3K pathway activation in ILC development.

t-MYPT1 and t-ASPP2 have differential effects on ILC progression

To investigate the impact of actomyosin relaxation on ILC progression, we determined the mammary tumor-related and overall survival of $WE^{F/F}$;t-MYPT1 and $WE^{F/F}$;t-ASPP2 mice (Fig. 4a, b and Supplementary Fig. 5a). Despite rapid onset of tumorigenesis, tumor-related survival and overall survival of $WE^{F/F}$;t-MYPT1 female mice was comparable to both $WE^{F/+}$;t-MYPT1 and $WE^{F/F}$ control mice (Fig. 4a and Supplementary Fig. 5a, b). Similar to $WE^{F/F}$ control mice, the majority of $WE^{F/F}$;t-MYPT1 mice were sacrificed due to aging-associated, non-tumor-related reasons. In contrast, the vast majority of $WE^{F/F}$;t-ASPP2 and $WE^{F/+}$;t-ASPP2 mice had to be sacrificed because tumor-related end points were met, resulting in significantly reduced tumor-related and overall survival compared to control mice (Fig. 4a, b and Supplementary Fig. 5a, b). Increased bioluminescence activity underscored the increased mammary tumor growth in $WE^{F/F}$;t-ASPP2 mice, compared to $WE^{F/F}$;t-MYPT1 mice (Supplementary Fig. 1 c). To ascertain if the difference in tumor-related survival between $WE^{F/F}$;t-MYPT1 and $WE^{F/F}$;t-ASPP2 mice was due to increased proliferation, we determined the amount of Ki67 positive tumor cells using IF analysis (Fig. 4c and d). The percentage of Ki67 positive tumor cells ($K8^{+}$;$Ecad^{-}$) in tumors from $WE^{F/F}$;t-ASPP2 mice was on average twofold higher than in tumors from $WE^{F/F}$;t-MYPT1 mice (Fig. 4d). This difference could be due to the fact that t-ASPP2 has retained the YAP binding domain (Fig. 1a). Indeed, previous work has shown that ASPP2 can drive both YAP and TAZ dephosphorylation, enabling nuclear localization and transcriptional activation[16,17]. We therefore tested if t-ASPP2

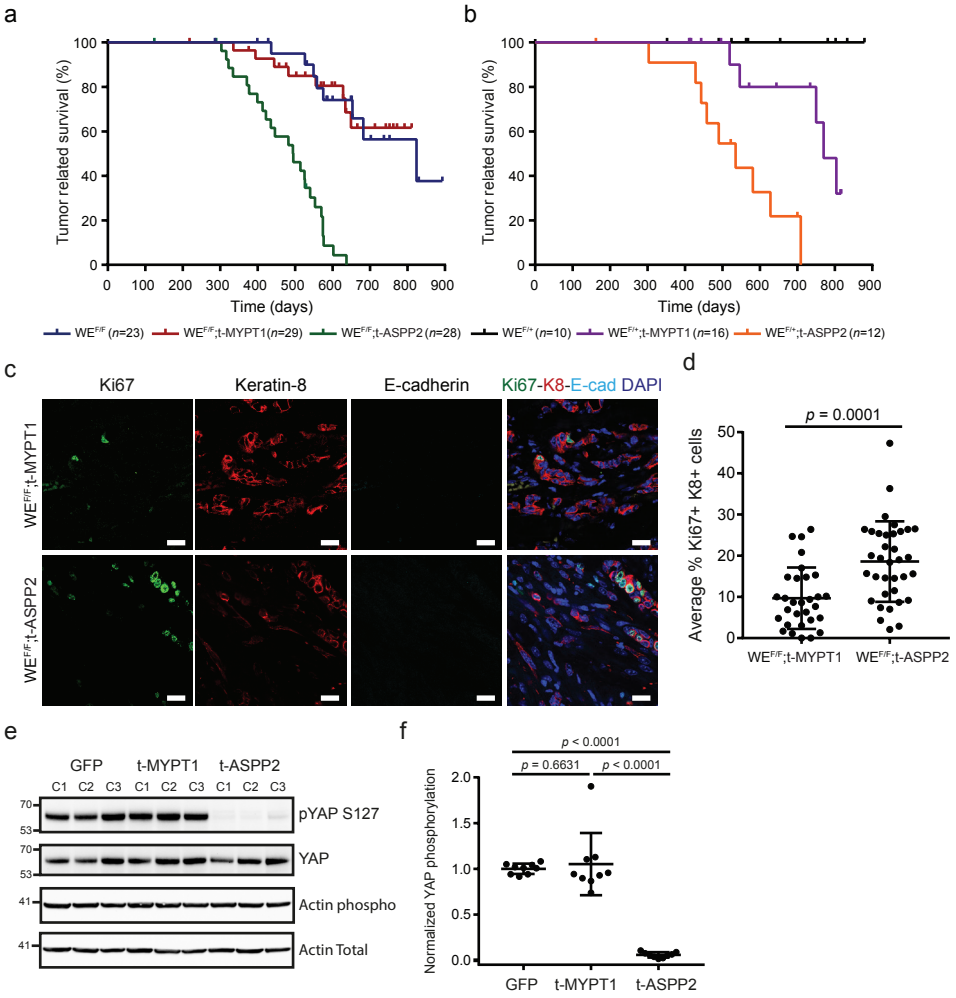

Figure 4: t-MYPT1 and t-ASPP2 have differential effects on ILC progression (**a**, **b**) Kaplan–Meier curves showing mammary tumor-related survival for female mice with the indicated genotypes. (**c**, **d**) Representative images (**c**) and quantifications (**d**)**,** of IF staining in tumors WE$^{F/F}$;t-MYPT1 and WE$^{F/F}$;t-ASPP2 mice stained for, Ki67 (green), Cytokeratin 8 (Red) and E-cadherin (Cyan). Scale bars are 20 µm. (**e**, **f**) Representative images (**e**) and quantification (**f**) of Western blot analysis of WE$^{F/F}$;*mTmG* MMECs transduced with t-ASPP2, t-MYTP1 or GFP stained for YAP, phosphorylated YAP (serine 127) and actin.

can dephosphorylate and thereby activate YAP. Western blot analysis of E-cadherin-deficient MMECs overexpressing t-ASPP2, t-MYPT1 or GFP showed that only t-ASPP2 causes near complete dephosphorylation of YAP on Serine 127 (Fig. 4e and f). Overall, these results indicate that t-ASPP2 promotes ILC progression via YAP activation.

YAP activation by t-ASPP2 is not required for cell adhesion and survival of E-cadherin-deficient MMECs

To determine if activation of YAP by t-ASPP2 is required for increased adhesion and survival of E-cadherin-deficient MMECs, we generated a t-ASPP2 point mutant ,t-ASPP2$^{\Delta YAP}$, in which the YAP binding motif PPXY[41] is mutated (Fig. 5a). Western blot analysis showed that t-ASPP2$^{\Delta YAP}$ is expressed at levels comparable to t-ASPP2 but no longer causes dephosphorylation of YAP at serine 127 (Fig. 5b and c). We next assessed whether the lack of YAP activity had any effect on the ability of t-ASPP2 to promote adhesion and survival of E-cadherin-deficient MMECs. Colony formation assays with E-cadherin-deficient MMECs overexpressing t-ASPP2$^{\Delta YAP}$, t-ASPP2 and GFP showed that both t-ASPP2 and t-ASPP2$^{\Delta YAP}$ promote survival of cells upon withdrawal of ROCK inhibitor (Fig. 5d, e). Furthermore, t-ASPP2$^{\Delta YAP}$ induced MLC dephosphorylation to the same level as t-ASPP2, indicating that this activity is independent of YAP (Fig. 5f and g). To determine if the effect of t-ASPP2 on actomyosin relaxation was dependent on PP1 binding, we generated a second t-ASPP2 point mutant, t-ASPP2$^{\Delta PP1}$, that can no longer bind PP1 (Supplementary Fig. 6a)[17]. Expression of t-ASPP2$^{\Delta PP1}$ no longer resulted in actomyosin relaxation nor did this mutant dephosphorylate YAP (Supplementary Fig. 6 b-e). Expression of t-ASPP2$^{\Delta PP1}$ also did not promote adhesion and survival of E-cadherin-deficient MMECs (Supplementary Fig. 6f, g). Together, these data show that the ability of t-ASPP2 to drive actomyosin relaxation and thereby promote adhesion/survival of E-cadherin-deficient MMECs is mediated by PP1 but not by YAP activation.

YAP activation by t-ASPP2 is not required for tumor initiation but promotes tumor growth

To determine the contribution of t-ASPP2-mediated YAP activation to ILC initiation and progression, we made use of a second truncation variant of ASPP2 (t2-ASPP2) that lacks exons 1-13 (Fig. 6a). Similar to t-ASPP2$^{\Delta YAP}$, expression of t2-ASPP2 causes actomyosin relaxation and enables adhesion and survival of E-cadherin-deficient MMECs, but does not result in YAP activation, (Supplementary Fig. 7a-f). We performed intraductal injections with lentiviruses encoding t-ASPP2, t2-ASPP2 and empty control in the mammary glands of 6- to 8-week-old WE$^{F/F}$ mice (Fig. 6b). Twenty weeks post injection, we isolated the injected mammary glands and checked for the presence and size of any developed tumors. Similar to the

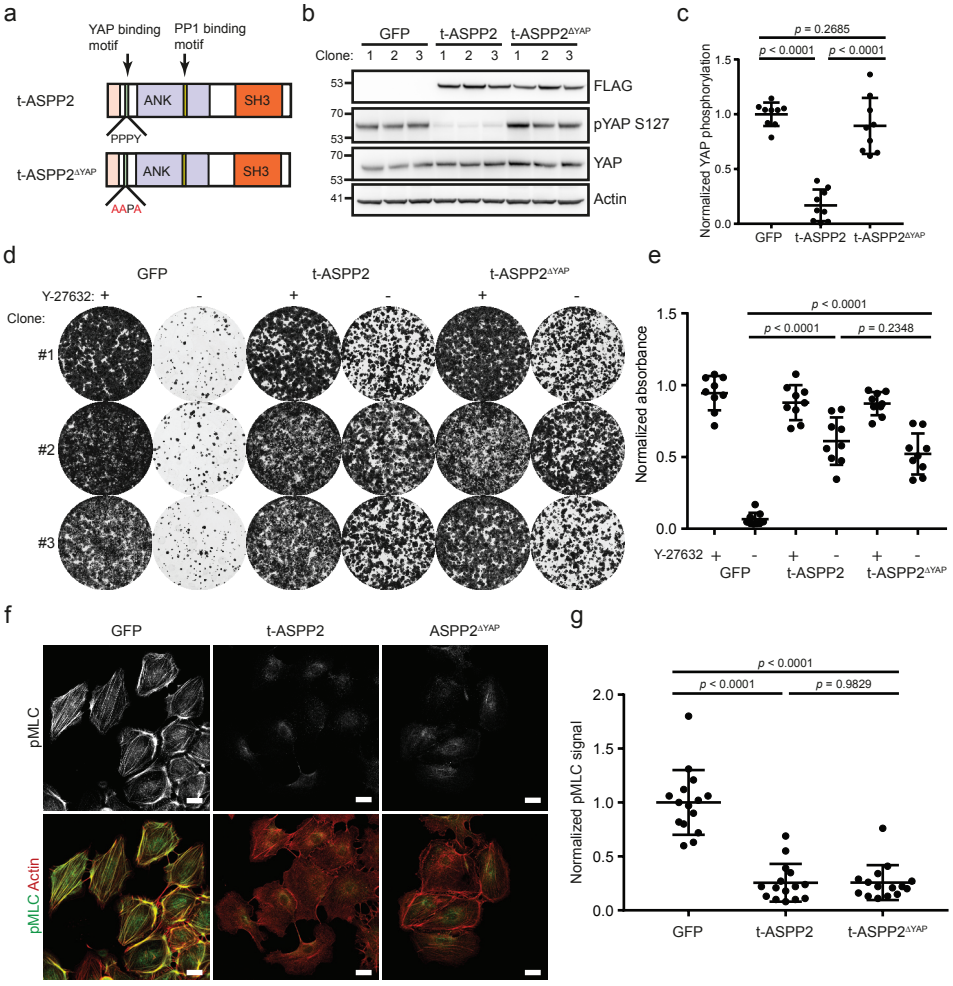

Figure 5: YAP activation by t-ASPP2 is not required for cell adhesion and survival of E-cadherin deficient MMECs. (**a**) Schematic overview of t-ASPP2 and t-ASPP2$^{\Delta YAP}$ showing the ankyrin repeats (purple), PP1 binding motif(yellow), SH3 domain (red), YAP binding domain (green) and proline rich domain in (light pink). (B, C) Representative images (**b**) and quantification (**c**) of Western blot analysis of WE$^{F/F}$;*mTmG* MMECs transduced with t-ASPP2, t-ASPP2$^{\Delta YAP}$ or GFP stained for YAP, phosphorylated YAP (serine^{127}) and actin. (**d**, **e**) Representative images (**d**) and quantification (e) of clonogenic assays with WE$^{F/F}$;*mTmG* MMECs transduced with t-ASPP2, t-ASPP2$^{\Delta YAP}$ or GFP 7 days post seeding in the presence or absence of 10 μM Y-27632. (**f**, **g**) IF staining (**f**) and quantification (**g**) of WE$^{F/F}$;*mTmG* MMECs transduced with t-ASPP2, t-ASPP2$^{\Delta YAP}$ or GFP 48 hours post washout of 10 μM Y-27632 stained for phospho myosin light chain (serine 19), actin and Hoechst. Scale bar is 25 μm.

results shown in Figure 2, all glands injected with the empty vector were tumor-free, whereas all glands injected with t-ASPP2 contained tumors (Fig. 6c). Nine out of ten glands injected with t2-ASPP2 contained tumors

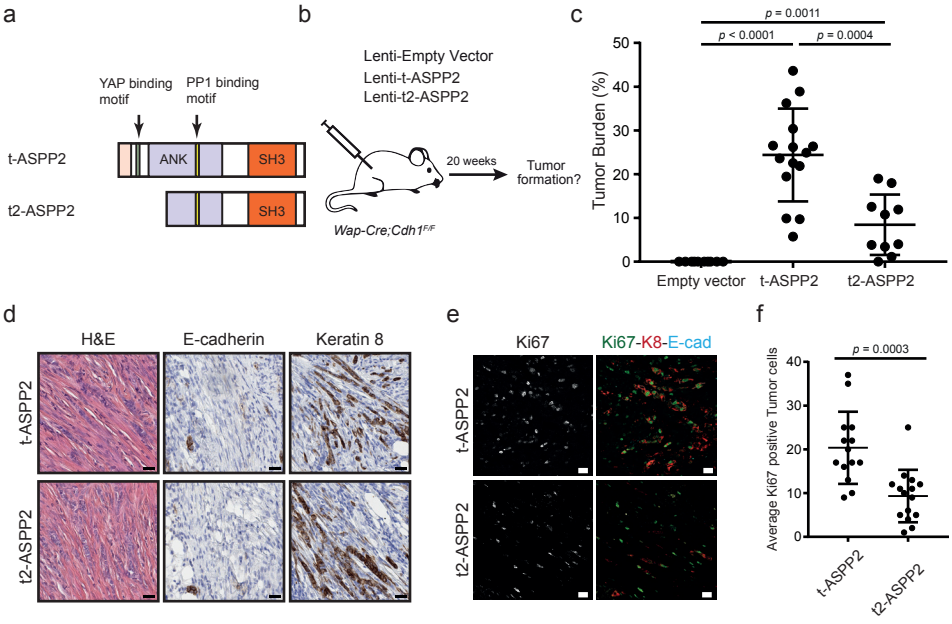

Figure 6: YAP activation by t-ASPP2 is not required for tumor initiation but promotes tumor growth (**a**) Schematic overview of t-ASPP2 and t2-ASPP2 showing the ankyrin repeats (purple), PP1 binding motif (yellow), SH3 domain (red), YAP binding domain (green) and proline rich domain in (light pink) (**b**) Schematic representation of Intraductal injections performed in $WE^{F/F}$ animals with high titer lenti-virus containing a vector encoding t-ASPP2, t2-ASPP2. (**c**) Tumor burden of $WE^{F/F}$ females 20 weeks after injection Empty vector lenti-viruses (*n* = 10 glands) or viruses containing t-ASPP2 (*n* = 15 glands) or t2-ASPP2 (*n* = 10 glands). (**d**) Representative images for H&E staining (left) and for expression of E-cadherin (middle) and CK8 (right) in tumors. Scale bars are 20 µM. (**e**) Representative imaging of IF staining of tumors generated by injection of t-ASPP2 or t2-ASPP2 stained for, Ki67 (green), Cytokeratin 8 (Red) and E-cadherin (Cyan). Scale bars are 25 µm. (**f**) Quantification of the number of Ki67 positive tumor ($CK8^{pos}$, $E\text{-}cad^{neg}$) in t-ASPP2 or t2-ASPP2 induced tumors (*n* = 3 glands (5 images/gland)).

but the size of these tumors was substantially reduced (Fig. 6c). Similar to the t-ASPP2-induced tumors, the morphology of tumors induced by injection of t2-ASPP2 resembled classic ILC (Fig. 6d). To assess whether the differential effect of t-ASPP2 and t2-ASPP2 on tumor growth was reflected by differences in proliferation, we quantified the amount of Ki67-positive tumors cells (Fig. 6e and f). Tumors driven by t2-ASPP2 had on average half the amount of Ki67 positive tumor cells compared to tumors driven by t-ASPP2. Together, these data indicate that YAP activation induced by t-ASPP2 is not required for tumor initiation but does lead to enhanced proliferation and tumor growth.

Discussion

The discovery of ASPP2 as a binding partner of p53 sparked extensive research into the tumor suppressive roles of ASPP2. It has become clear that ASPP2 not only facilitates apoptosis but also inhibits cell proliferation and metastasis[27,42,43]. In contrast, recent work has shown that dominant-negative variants of ASPP2, or dominant-active variants that lack the tumor suppressive functions of ASPP2, can also have oncogenic roles in various cancer types[14,44,45]. Van Hook et al. showed that a truncation variant of ASPP2 that uses an alternative transcriptional start site in exon 8 is overexpressed in human breast cancers[44]. Similar to the truncation variant investigated by van Hook et al., the ASPP2 truncation variant investigated in this study lacks the N-terminus, indicating both variants may promote tumorigenesis via similar mechanisms. However, it remains to be determined whether the truncation variant identified by van Hook et al. is expressed in ILC patients. We have previously shown that expression of t-ASPP2 does not dampen p53 activation, indicating that it does not act as a dominant-negative version of wild-type ASPP2[14].

This study demonstrates that overexpression of t-ASPP2 results in actomyosin relaxation, thereby enabling adhesion and survival of E-cadherin-deficient MMECs *in vitro* and *in vivo*. The observation that inhibition of ROCK1/2 leads to tumor formation in $WE^{F/F}$ mice provides further evidence that actomyosin relaxation in E-cadherin-deficient MMECs is sufficient to drive ILC formation. Our results suggest that t-ASPP2 has dominant-active functions since it induces MLC dephosphorylation comparable to t-MYPT1, which is considered dominant-active since it lacks the inhibitory phosphorylation sites targeted by Rho Kinases ROCK1 and ROCK2[5]. The dominant-active function of t-ASPP2 may be explained by the lack of the proline rich domain which has been shown inhibit ASPP2 protein-protein interactions by shielding the PP1 interaction domain[22]. Our data show that t-ASPP2 requires the interaction with PP1 to induce MLC dephosphorylation and that this function is not dependent on YAP activation. Together, these results suggest that t-ASPP2 might dephosphorylate MLC directly, which is a function not yet attributed to ASPP2.

Besides E-cadherin loss, the most frequently mutated pathway in human ILC is the PI3 kinase pathway[9,38,39]. PI3K pathway mutations can indirectly control actomyosin contractility by activation of the Rho GTPase RAC1, leading to inhibition of Rho kinase[46,47]. The observation that both t-MYPT1

and t-ASPP2 collaborate with loss of PTEN and E-cadherin in ILC formation indicates that PI3K pathway activation does not induce actomyosin relaxation, although it remains possible that mutations in PIK3CA have different effects on actomyosin contractility, compared to PTEN loss.

Previous work has shown that ASPP2 can dephosphorylate YAP and thereby induce YAP-mediated transcription[16,17]. Our study shows that t-ASPP2-mediated YAP activation is not required for adhesion and survival of E-cadherin-deficient MMECs. YAP activation was also not required for tumor initiation but did enhance tumor growth and enhanced tumor progression. Intriguingly, nuclear localization of YAP is also substantially more frequent in ILCs compared to invasive ductal carcinomas, which is thought to be due to lack of intact adherens junctions[48]. However, YAP phosphorylation is still very prevalent in E-cadherin-deficient MMECs, which have no adherens junctions, indicating that loss of E-cadherin alone does not result in complete YAP activation. Of note, higher levels of YAP activation in human ILCs might also be explained by the frequent amplification of *ASPP2* in these tumors[14].

In this study we confirmed our previous observation that actomyosin relaxation gives rise to rapid tumor formation in mice when combined with loss of E-cadherin[14,5]. Near identical tumor latencies in $WE^{F/F}$;t-MYPT1 and $WE^{F/F}$;t-ASPP2 mice suggest that YAP activation driven by t-ASPP2 does not play a notable role in ILC initiation. On the other hand, growth and progression of ILCs appears to be enhanced by YAP activation as nearly all $WE^{F/F}$;t-ASPP2 mice had to be sacrificed due to tumor-related endpoints. The fact that most $WE^{F/F}$;t-MYPT1 mice had to be culled due to non-tumor-related events indicates that ILCs driven by combined loss of E-cadherin and actomyosin relaxation progress very slowly, thus mimicking human ILCs, which generally also have a low proliferation and metabolism[49–51].

In conclusion, we have shown that t-ASPP2 causes both actomyosin relaxation and YAP activation. Whereas actomyosin relaxation drives adhesion and survival of E-cadherin-deficient MMECs and leads to ILC development, YAP activation causes enhanced tumor-growth and progression. These new insights in the different mechanisms through which t-ASPP2 drives ILC initiation and progression advance our understanding of ILC development and may ultimately contribute to novel therapeutic opportunities for ILC patients.

Authors' Contributions

Conception and design: K. Schipper, M. Nethe, J. Jonkers

Development of methodology: K. Schipper, M. Nethe, J. Jonkers

Acquisition of data (provided animals, acquired and managed patients, provided facilities, etc.): K. Schipper, S.P. Cornelissen, A.P. Drenth, E. van der Burg, S. Klarenbeek, M. Nethe

Analysis and interpretation of data (e.g., statistical analysis, biostatistics, computational analysis): K. Schipper, S.P. Cornelissen, S. Klarenbeek, M. Nethe, J. Jonkers

Writing, review, and/or revision of the manuscript: K. Schipper, M. Nethe, J. Jonkers

Administrative, technical, or material support (i.e., reporting or organizing data, constructing databases): A.P. Drenth, E. van der Burg

Study supervision: M. Nethe, J. Jonker

Acknowledgements

We are grateful to Stefano Annunziato for providing technical suggestions and help with the experiments. We thank the NKI animal facility, the animal pathology facility, the transgenic facility and the intervention unit of the NKI mouse clinic, and the digital microscopy facility for their expert technical support. Financial support was provided by the Dutch Cancer society (KWF project 2015-7589), the European Research Council (ERC Synergy project CombatCancer 319661), the Netherlands Organization for Scientific Research (NWO: Cancer Genomics Netherlands (CGCNL), VENI 016156012 (M.N.) and VICI 91814643 (J.J)). This work is part of the Oncode Institute which is partly financed by the Dutch Cancer Society.

Supplementary Figures

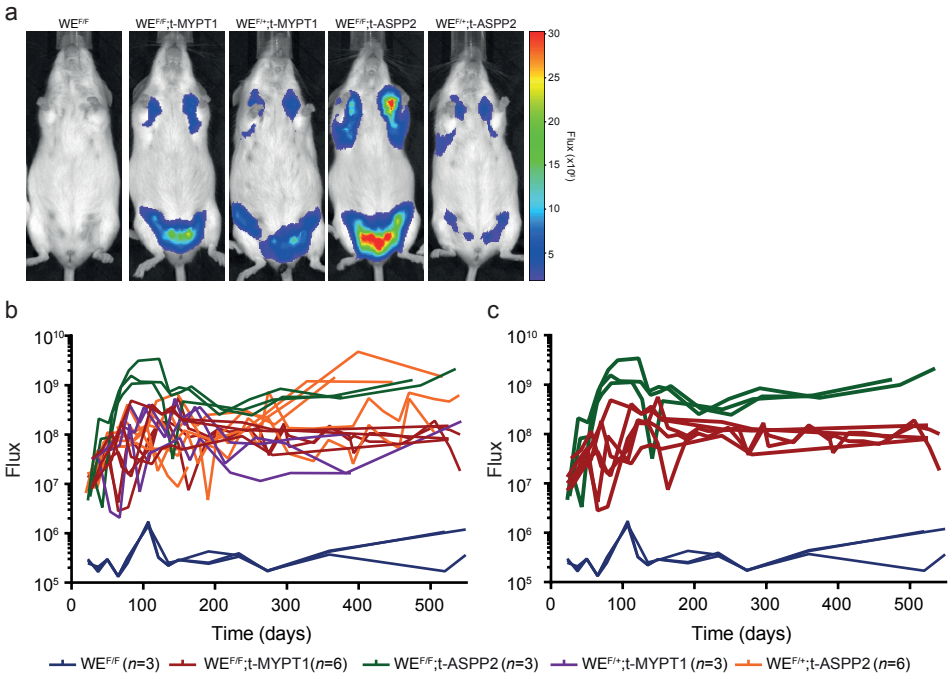

Supplementary Figure 1: In vivo bioluminescent imaging of WE$^{F/F}$;t-MYPT1 and WE$^{F/F}$;t-ASPP2 mice (**a**) Representative images of in vivo bioluminescence imaging of luciferase expression of WE$^{F/F}$;t-MYPT1 and WE$^{F/F}$;t-ASPP2 mice with the indicated genotypes at 100 days. (**b**, **c**) Quantifications of in vivo bioluminescence imaging of luciferase expression of WE$^{F/F}$;t-MYPT1 and WE$^{F/F}$;t-ASPP2 mice with the indicated genotypes.

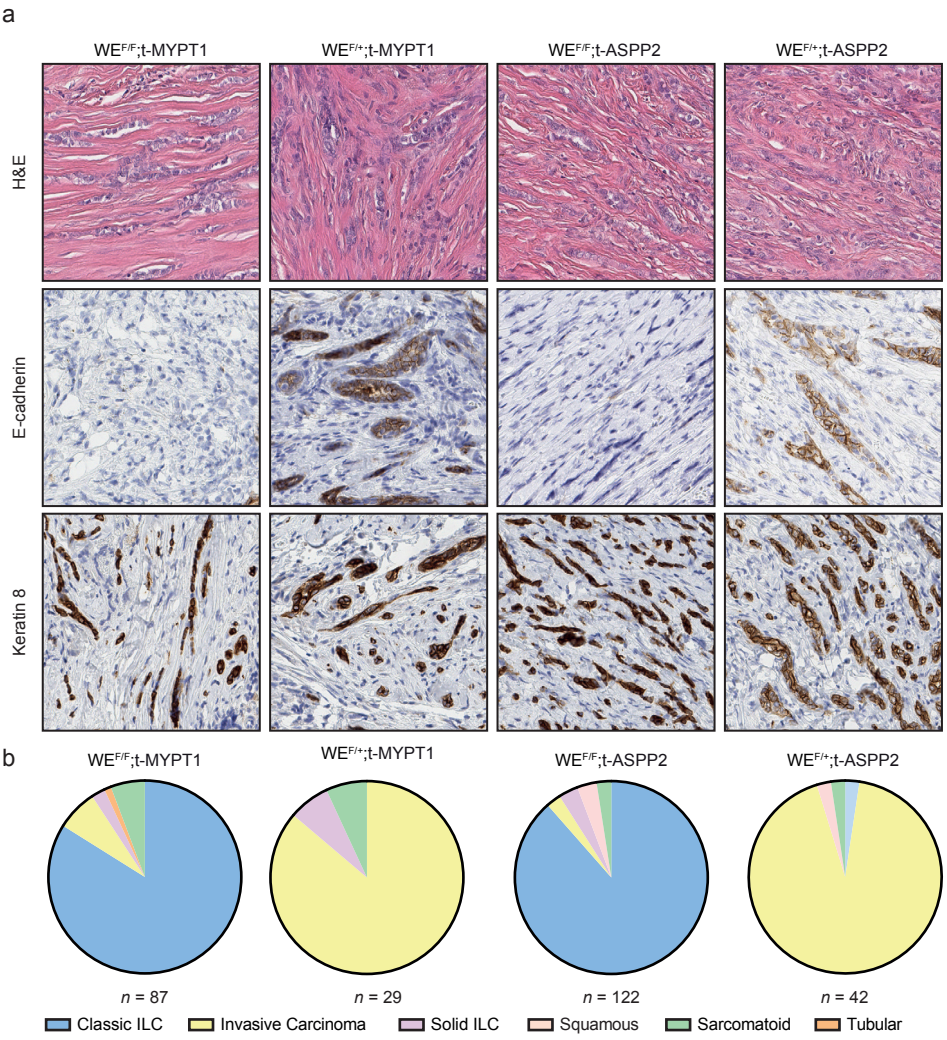

Supplementary Figure 2: Pathology analysis of WE$^{F/F}$;t-MYPT1 and WE$^{F/F}$;t-ASPP2 derived tumors (**a**) Representative images for H&E staining (top) and IHC staining of E-cadherin (middle) and CK8 (bottom) in tumors of WE$^{F/F}$;t-MYPT1 and WE$^{F/F}$;t-ASPP2 mice with the indicated genotypes. (**b**) Pie charts showing the distribution of mammary tumor phenotypes in WE$^{F/F}$;t-MYPT1 (*n* = 57), WE$^{F/+}$;t-MYPT1 (*n* = 24), WE$^{F/F}$;t-ASPP2 (*n* = 118), and WE$^{F/+}$;t-ASPP2 (*n* = 30) tumors. Scale bar is 20 µm.

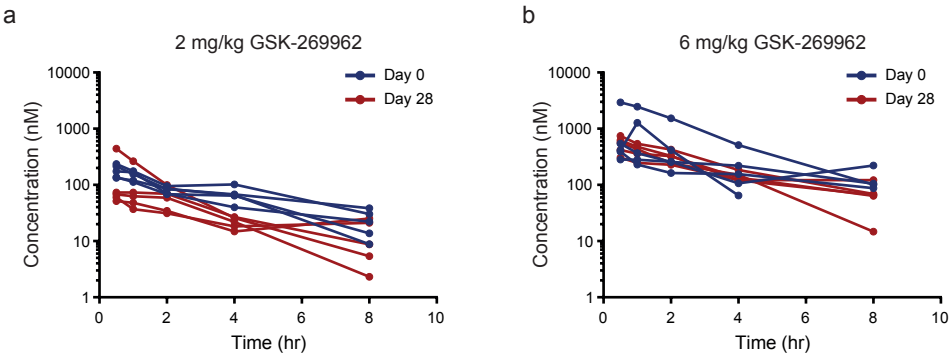

Supplementary Figure 3: Pharmacokinetics of GSK-269962 intervention study (**a, b**) Plasma concentrations of GSK-269962 at the indicated time points after oral administration of 2 (**a**), or 6 mg/kg GSK-269962 (**b**).

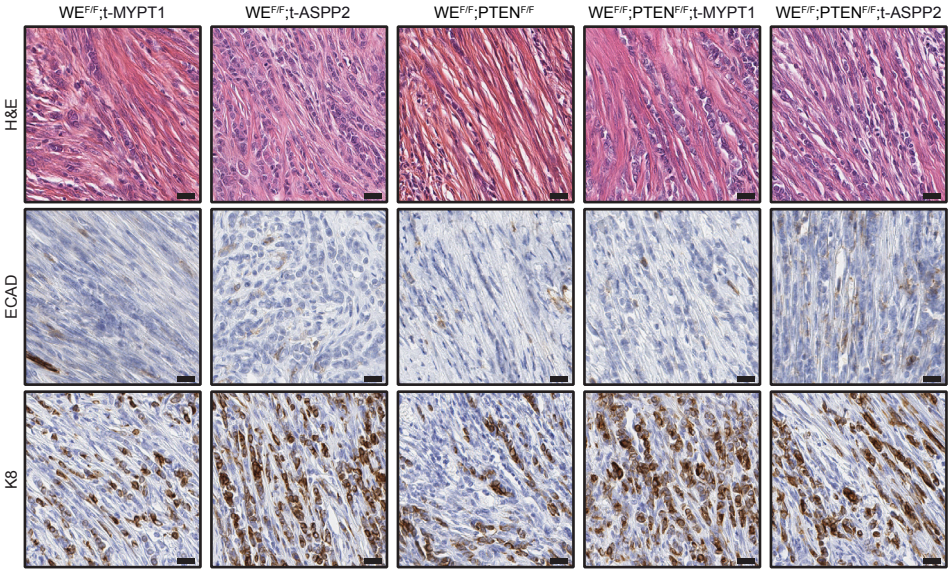

Supplementary Figure 4: Tumor morphology WE$^{F/F}$;PTEN$^{F/F}$;t-MYPT1 and WE$^{F/F}$;PTEN$^{F/F}$;t-ASPP2 mice Representative images for H&E staining (top) and IHC staining of E-cadherin (middle) and CK8 (bottom) in tumors of from 20 week old female mice with the indicated genotypes. Scale bar is 20 µm.

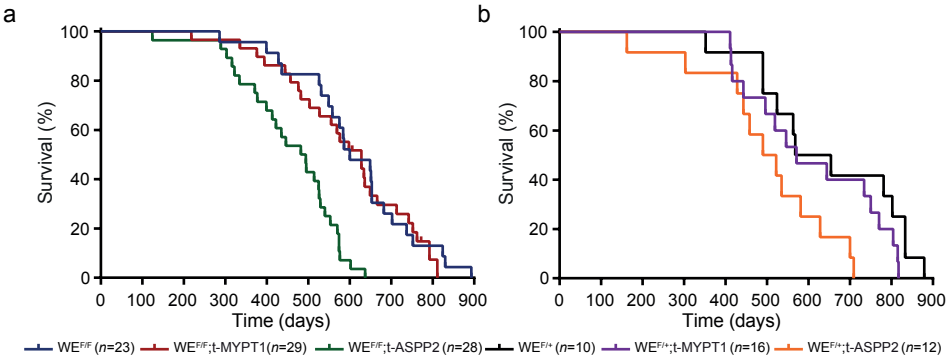

Supplementary Figure 5: Overall survival analysis of WE$^{F/F}$;t-MYPT1 and WE$^{F/F}$;t-ASPP2 mice (**a, b**) Kaplan–Meier curves showing overall survival for female mice with the indicated genotypes.

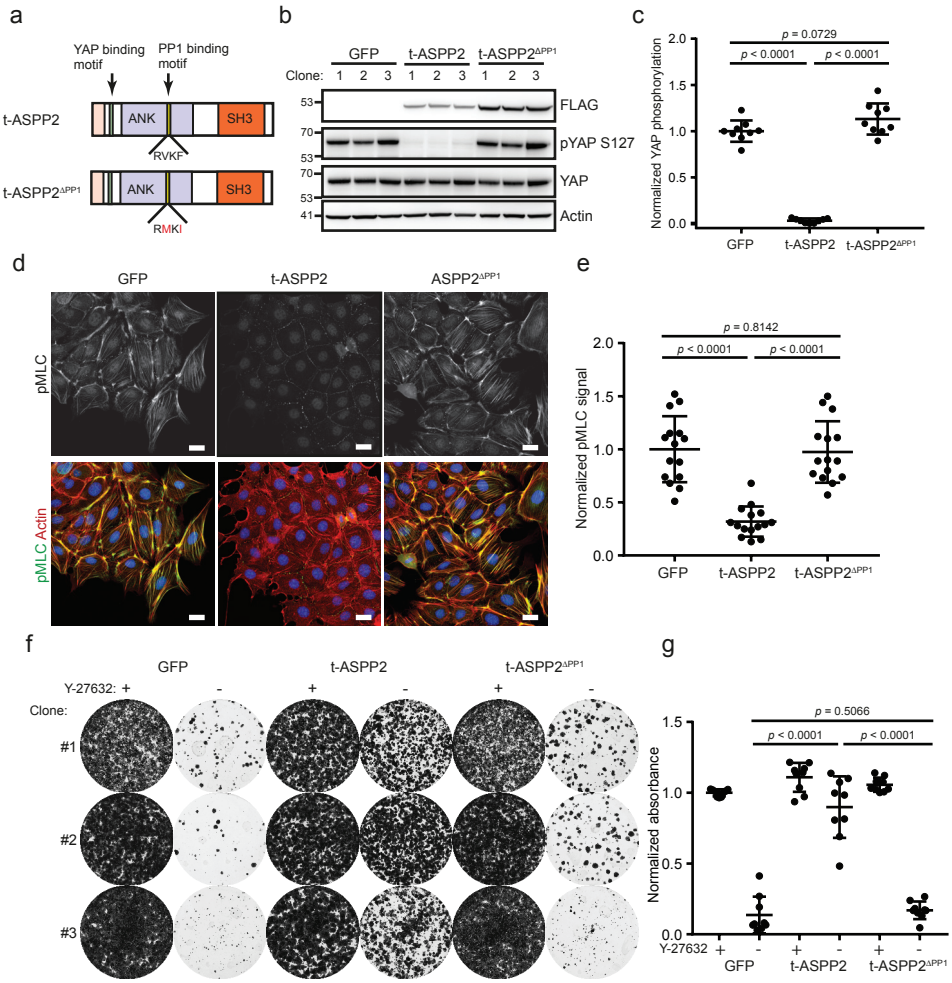

Supplementary Figure 6: Interaction of t-ASPP2 with PP1 is required for cell adhesion and survival of E-cadherin deficient MMECs (**a**) Schematic overview of t-ASPP2 and t-ASPP2$^{\Delta PP1}$ showing the ankyrin repeats (purple), PP1 binding motif(yellow), SH3 domain (red), YAP binding domain (green) and proline rich domain in (light pink). The mutated residues are shown in red. (**b**, **c**) Representative images (**b**) and quantification (**c**) of Western blot analysis of WE$^{F/F}$;*mTmG* MMECs transduced with t-ASPP2, t-ASPP2$^{\Delta PP1}$ or GFP stained for YAP, phosphorylated YAP (serine 127) and actin. (D,E) IF staining (**d**) and quantification (**e**) of WE$^{F/F}$;*mTmG* MMECs transduced with t-ASPP2, t-ASPP2$^{\Delta PP1}$ or GFP 48 hours post washout of 10 μM Y-27632 stained for phospho myosin light chain (Serine 19), actin and Hoechst. Scale bar is 25 μm. (**f**, **g**) Representative images (**f**) and quantification (**g**) of clonogenic assays with WE$^{F/F}$;*mTmG* MMECs transduced with t-ASPP2, t-ASPP2$^{\Delta PP1}$ or GFP 7 days post seeding in the presence or absence of 10 μM Y-27632.

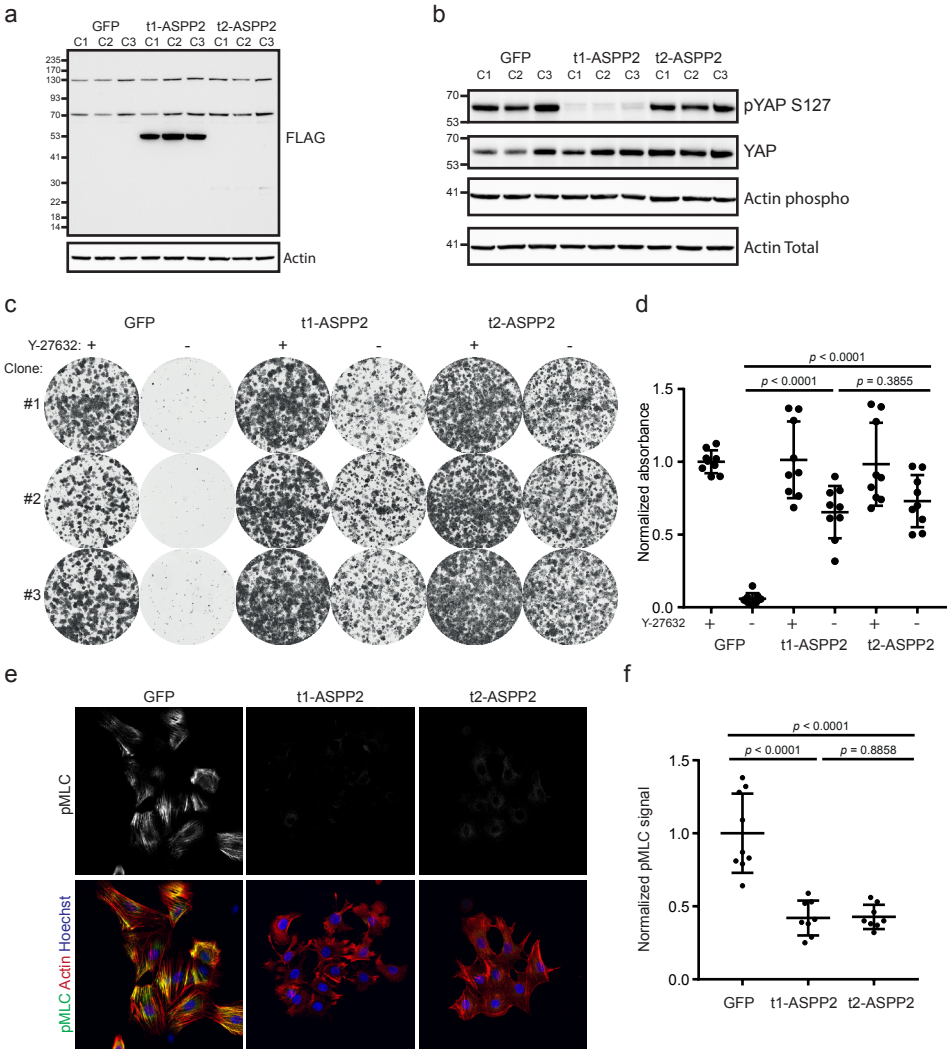

Supplementary Figure 7: t2-ASPP2 induces actomyosin relaxation enabling adhesion and survival of E-cadherin-deficient MMECs (**a**) Western blot analysis of WE$^{F/F}$;*mTmG* MMECs transduced with t-ASPP2, t2-ASPP2 or GFP stained for FLAG (**b, c**) Western blot analysis showing Representative images (**b**) and quantification (**c**) of WE$^{F/F}$;*mTmG* MMECs transduced with t-ASPP2, t2-ASPP2 or GFP stained for YAP, phosphorylated YAP (serine 127) and actin. (**d**, **e**) Representative images (**d**) and quantification (**e**) of clonogenic assays with WE$^{F/F}$;*mTmG* MMECs transduced with t-ASPP2, t2-ASPP2 or GFP 7 days post seeding in the presence or absence of 10 μM Y-27632. (**f**, **g**) IF staining (**f**) and quantification (**g**) of WE$^{F/F}$;*mTmG* MMECs transduced with t-ASPP2, t2-ASPP2 or GFP 48 hours post washout of 10 μM Y-27632 stained for phospho myosin light chain (Serine 19), actin and Hoechst. Scale bar is 25 μm.

Supplmentary tables (available online)

Supplementary Table 1

List of primers used for cloning and genotyping

Supplementary Table 2

GSK-296692 intervention study dosing overview

Supplementary Table 3

Criteria for histopathological classification of tumors

References

1. Martinez, V. & Azzopardi, J. G. Invasive lobular carcinoma of the breast: incidence and variants. *Histopathology* 3, 467–488 (1979).

2. Arpino, G., Bardou, V. J., Clark, G. M. & Elledge, R. M. Infiltrating lobular carcinoma of the breast: tumor characteristics and clinical outcome. *Breast Cancer Res. BCR* 6, R149-156 (2004).

3. Wong, H. *et al.* Lobular breast cancers lack the inverse relationship between ER/PR status and cell growth rate characteristic of ductal cancers in two independent patient cohorts: implications for tumor biology and adjuvant therapy. *BMC Cancer* 14, 826 (2014).

4. Vos, C. B. *et al.* E-cadherin inactivation in lobular carcinoma in situ of the breast: an early event in tumorigenesis. *Br. J. Cancer* 76, 1131–1133 (1997).

5. Schipper, K. *et al.* Rebalancing of actomyosin contractility enables mammary tumor formation upon loss of E-cadherin. *Nat. Commun.* 10, 3800 (2019).

6. Porter, A. J., Evans, E. B., Foxcroft, L. M., Simpson, P. T. & Lakhani, S. R. Mammographic and ultrasound features of invasive lobular carcinoma of the breast. *J. Med. Imaging Radiat. Oncol.* 58, 1–10 (2014).

7. Moll, R., Mitze, M., Frixen, U. H. & Birchmeier, W. Differential loss of E-cadherin expression in infiltrating ductal and lobular breast carcinomas. *Am. J. Pathol.* 143, 1731–1742 (1993).

8. Rakha, E. A. *et al.* Clinical and biological significance of E-cadherin protein expression in invasive lobular carcinoma of the breast. *Am. J. Surg. Pathol.* 34, 1472–1479 (2010).

9. Ciriello, G. *et al.* Comprehensive Molecular Portraits of Invasive Lobular Breast Cancer. *Cell* 163, 506–519 (2015).

10. Boussadia, O., Kutsch, S., Hierholzer, A., Delmas, V. & Kemler, R. E-cadherin is a survival factor for the lactating mouse mammary gland. *Mech. Dev.* 115, 53–62 (2002).

11. Boelens, M. C. *et al.* PTEN Loss in E-Cadherin-Deficient Mouse Mammary Epithelial Cells Rescues Apoptosis and Results in Development of Classical Invasive Lobular Carcinoma. *Cell Rep.* 16, 2087–2101 (2016).

12. Derksen, P. W. B. *et al.* Somatic inactivation of E-cadherin and p53 in mice leads to metastatic lobular mammary carcinoma through induction of anoikis resistance and angiogenesis. *Cancer Cell* 10, 437–449 (2006).

13. Derksen, P. W. B. *et al.* Mammary-specific inactivation of E-cadherin and p53 impairs functional gland development and leads to pleomorphic invasive lobular carcinoma in mice. *Dis. Model. Mech.* 4, 347–358 (2011).

14. Kas, S. M. *et al.* Insertional mutagenesis identifies drivers of a novel oncogenic pathway in invasive lobular breast carcinoma. *Nat. Genet.* (2017) doi:10.1038/ng.3905.

15. Matsumura, F. & Hartshorne, D. J. Myosin phosphatase target subunit: Many roles in cell function. *Biochem. Biophys. Res. Commun.* 369, 149–156 (2008).

16. Liu, C.-Y. *et al.* PP1 Cooperates with ASPP2 to Dephosphorylate and Activate

TAZ. *J. Biol. Chem.* 286, 5558–5566 (2011).

17. Royer, C. *et al.* ASPP2 Links the Apical Lateral Polarity Complex to the Regulation of YAP Activity in Epithelial Cells. *PLoS ONE* 9, (2014).

18. Sullivan, A. & Lu, X. ASPP: a new family of oncogenes and tumour suppressor genes. *Br. J. Cancer* 96, 196–200 (2007).

19. Vicente-Manzanares, M., Ma, X., Adelstein, R. S. & Horwitz, A. R. Non-muscle myosin II takes centre stage in cell adhesion and migration. *Nat. Rev. Mol. Cell Biol.* 10, 778–790 (2009).

20. Schramek, D. *et al.* Direct in vivo RNAi screen unveils myosin IIa as a tumor suppressor of squamous cell carcinomas. *Science* 343, 309–313 (2014).

21. Conti, M. A. *et al.* Conditional deletion of nonmuscle myosin II-A in mouse tongue epithelium results in squamous cell carcinoma. *Sci. Rep.* 5, 14068 (2015).

22. Rotem, S. *et al.* The structure and interactions of the proline-rich domain of ASPP2. *J. Biol. Chem.* 283, 18990–18999 (2008).

23. Rotem-Bamberger, S., Katz, C. & Friedler, A. Regulation of ASPP2 Interaction with p53 Core Domain by an Intramolecular Autoinhibitory Mechanism. *PLOS ONE* 8, e58470 (2013).

24. Vlug, E., Ercan, C., van der Wall, E., van Diest, P. J. & Derksen, P. W. B. Lobular breast cancer: pathology, biology, and options for clinical intervention. *Arch. Immunol. Ther. Exp. (Warsz.)* 62, 7–21 (2014).

25. Iwabuchi, K., Bartel, P. L., Li, B., Marraccino, R. & Fields, S. Two cellular proteins that bind to wild-type but not mutant p53. *Proc. Natl. Acad. Sci. U. S. A.* 91, 6098–6102 (1994).

26. Thukral, S. K., Blain, G. C., Chang, K. K. & Fields, S. Distinct residues of human p53 implicated in binding to DNA, simian virus 40 large T antigen, 53BP1, and 53BP2. *Mol. Cell. Biol.* 14, 8315–8321 (1994).

27. Samuels-Lev, Y. *et al.* ASPP proteins specifically stimulate the apoptotic function of p53. *Mol. Cell* 8, 781–794 (2001).

28. Zhang, P. *et al.* ASPP1/2-PP1 complexes are required for chromosome segregation and kinetochore-microtubule attachments. *Oncotarget* 6, 41550–41565 (2015).

29. Wang, Y. *et al.* ASPP1 and ASPP2 bind active RAS, potentiate RAS signalling and enhance p53 activity in cancer cells. *Cell Death Differ.* 20, 525–534 (2013).

30. Sottocornola, R. *et al.* ASPP2 binds Par-3 and controls the polarity and proliferation of neural progenitors during CNS development. *Dev. Cell* 19, 126–137 (2010).

31. Henneman, L. *et al.* Selective resistance to the PARP inhibitor olaparib in a mouse model for BRCA1-deficient metaplastic breast cancer. *Proc. Natl. Acad. Sci. U. S. A.* 112, 8409–8414 (2015).

32. Krause, S., Brock, A. & Ingber, D. E. Intraductal injection for localized drug delivery to the mouse mammary gland. *J. Vis. Exp. JoVE* (2013) doi:10.3791/50692.

33. Annunziato, S. *et al.* Modeling invasive lobular breast carcinoma by CRISPR/Cas9-mediated somatic genome editing of the mammary gland. *Genes Dev.* 30, 1470–1480 (2016).

34. Montini, E. *et al.* The genotoxic potential of retroviral vectors is strongly modulated by vector design and integration site selection in a mouse model of HSC gene therapy. *J. Clin. Invest.* 119, 964–975 (2009).

35. Ito, M., Nakano, T., Erdodi, F. & Hartshorne, D. J. Myosin phosphatase: structure, regulation and function. *Mol. Cell. Biochem.* 259, 197–209 (2004).

36. Stavenger, R. A. *et al.* Discovery of aminofurazan-azabenzimidazoles as inhibitors of Rho-kinase with high kinase selectivity and antihypertensive activity. *J. Med. Chem.* 50, 2–5 (2007).

37. Feng, Y., LoGrasso, P. V., Defert, O. & Li, R. Rho Kinase (ROCK) Inhibitors and Their Therapeutic Potential. *J. Med. Chem.* 59, 2269–2300 (2016).

38. Desmedt, C. *et al.* Genomic Characterization of Primary Invasive Lobular Breast Cancer. *J. Clin. Oncol. Off. J. Am. Soc. Clin. Oncol.* 34, 1872–1881 (2016).

39. Michaut, M. *et al.* Integration of genomic, transcriptomic and proteomic data identifies two biologically distinct subtypes of invasive lobular breast cancer. *Sci. Rep.* 6, 18517 (2016).

40. An, Y. *et al.* Cdh1 and Pik3ca Mutations Cooperate to Induce Immune-Related Invasive Lobular Carcinoma of the Breast. *Cell Rep.* 25, 702-714.e6 (2018).

41. Espanel, X. & Sudol, M. Yes-associated protein and p53-binding protein-2 interact through their WW and SH3 domains. *J. Biol. Chem.* 276, 14514–14523 (2001).

42. Wang, Y. *et al.* ASPP2 controls epithelial plasticity and inhibits metastasis through β-catenin-dependent regulation of ZEB1. *Nat. Cell Biol.* 16, 1092–1104 (2014).

43. Katz, C. *et al.* Molecular basis of the interaction between the antiapoptotic Bcl-2 family proteins and the proapoptotic protein ASPP2. *Proc. Natl. Acad. Sci. U. S. A.* 105, 12277–12282 (2008).

44. Van Hook, K. *et al.* ΔN-ASPP2, a novel isoform of the ASPP2 tumor suppressor, promotes cellular survival. *Biochem. Biophys. Res. Commun.* 482, 1271–1277 (2017).

45. Schittenhelm, M. M. *et al.* Alternative splicing of the tumor suppressor ASPP2 results in a stress-inducible, oncogenic isoform prevalent in acute leukemia. *EBioMedicine* 42, 340–351 (2019).

46. Cain, R. J. & Ridley, A. J. Phosphoinositide 3-kinases in cell migration. *Biol. Cell* 101, 13–29 (2009).

47. Guilluy, C., Garcia-Mata, R. & Burridge, K. Rho protein crosstalk: another social network? *Trends Cell Biol.* 21, 718–726 (2011).

48. Vlug, E. J. *et al.* Nuclear localization of the transcriptional coactivator YAP is associated with invasive lobular breast cancer. *Cell. Oncol. Dordr.* 36, 375–384 (2013).

49. Du, T. *et al.* Invasive lobular and ductal breast carcinoma differ in immune response, protein translation efficiency and metabolism. *Sci. Rep.* 8, 7205

(2018).

50. Fujii, T. *et al.* Clinical Significance of 18F-FDG-PET in Invasive Lobular Carcinoma. *Anticancer Res.* 36, 5481–5485 (2016).

51. Groheux, D. *et al.* Correlation of high 18F-FDG uptake to clinical, pathological and biological prognostic factors in breast cancer. *Eur. J. Nucl. Med. Mol. Imaging* 38, 426–435 (2011).